Joint aperture detection for speckle reduction and increased collection efficiency in ophthalmic MHz OCT

Thomas Klein, Raphael André, Wolfgang Wieser, Tom Pfeiffer, and Robert Huber[*]

Lehrstuhl für BioMolekulare Optik, Fakultät für Physik, Ludwig-Maximilians-Universität München, Oettingenstr. 67, 80538 Munich, Germany
*Robert.Huber@LMU.de

Abstract: Joint-aperture optical coherence tomography (JA-OCT) is an angle-resolved OCT method, in which illumination from an active channel is simultaneously probed by several passive channels. JA-OCT increases the collection efficiency and effective sensitivity of the OCT system without increasing the power on the sample. Additionally, JA-OCT provides angular scattering information about the sample in a single acquisition, so the OCT imaging speed is not reduced. Thus, JA-OCT is especially suitable for ultra high speed in-vivo imaging. JA-OCT is compared to other angle-resolved techniques, and the relation between joint aperture imaging, adaptive optics, coherent and incoherent compounding is discussed. We present angle-resolved imaging of the human retina at an axial scan rate of 1.68 MHz, and demonstrate the benefits of JA-OCT: Speckle reduction, signal increase and suppression of specular and parasitic reflections. Moreover, in the future JA-OCT may allow for the reconstruction of the full Doppler vector and tissue discrimination by analysis of the angular scattering dependence.

OCIS codes: (170.4500) Optical coherence tomography; (170.3880) Medical and biological imaging; (120.3890) Medical optics instrumentation; (030.6140) Speckle.

References and links

1. D. Huang, E. A. Swanson, C. P. Lin, J. S. Schuman, W. G. Stinson, W. Chang, M. R. Hee, T. Flotte, K. Gregory, C. A. Puliafito, and J. G. Fujimoto, "Optical coherence tomography," Science **254**(5035), 1178–1181 (1991).
2. E. A. Swanson, J. A. Izatt, M. R. Hee, D. Huang, C. P. Lin, J. S. Schuman, C. A. Puliafito, and J. G. Fujimoto, "In vivo retinal imaging by optical coherence tomography," Opt. Lett. **18**(21), 1864–1866 (1993).
3. A. F. Fercher, C. K. Hitzenberger, W. Drexler, G. Kamp, and H. Sattmann, "In vivo optical coherence tomography," Am. J. Ophthalmol. **116**(1), 113–114 (1993).
4. C. A. Puliafito, M. R. Hee, C. P. Lin, E. Reichel, J. S. Schuman, J. S. Duker, J. A. Izatt, E. A. Swanson, and J. G. Fujimoto, "Imaging of macular diseases with optical coherence tomography," Ophthalmology **102**(2), 217–229 (1995).
5. W. Drexler and J. G. Fujimoto, "State-of-the-art retinal optical coherence tomography," Prog. Retin. Eye Res. **27**(1), 45–88 (2008).
6. M. Wojtkowski, B. Kaluzny, and R. J. Zawadzki, "New directions in ophthalmic optical coherence tomography," Optom. Vis. Sci. **89**(5), 524–542 (2012).
7. B. Golubovic, B. E. Bouma, G. J. Tearney, and J. G. Fujimoto, "Optical frequency-domain reflectometry using rapid wavelength tuning of a Cr^{4+}:forsterite laser," Opt. Lett. **22**(22), 1704–1706 (1997).
8. M. Choma, M. Sarunic, C. Yang, and J. Izatt, "Sensitivity advantage of swept source and Fourier domain optical coherence tomography," Opt. Express **11**(18), 2183–2189 (2003).
9. W. Drexler, "Ultrahigh-resolution optical coherence tomography," J. Biomed. Opt. **9**(1), 47–74 (2004).
10. M. Wojtkowski, V. Srinivasan, T. Ko, J. Fujimoto, A. Kowalczyk, and J. Duker, "Ultrahigh-resolution, high-speed, Fourier domain optical coherence tomography and methods for dispersion compensation," Opt. Express **12**(11), 2404–2422 (2004).
11. R. J. Zawadzki, S. M. Jones, S. S. Olivier, M. Zhao, B. A. Bower, J. A. Izatt, S. Choi, S. Laut, and J. S. Werner, "Adaptive-optics optical coherence tomography for high-resolution and high-speed 3D retinal in vivo imaging," Opt. Express **13**(21), 8532–8546 (2005).
12. Y. Zhang, J. Rha, R. Jonnal, and D. Miller, "Adaptive optics parallel spectral domain optical coherence tomography for imaging the living retina," Opt. Express **13**(12), 4792–4811 (2005).

13. K. Kurokawa, D. Tamada, S. Makita, and Y. Yasuno, "Adaptive optics retinal scanner for one-micrometer light source," Opt. Express **18**(2), 1406–1418 (2010).
14. B. Hermann, E. J. Fernández, A. Unterhuber, H. Sattmann, A. F. Fercher, W. Drexler, P. M. Prieto, and P. Artal, "Adaptive-optics ultrahigh-resolution optical coherence tomography," Opt. Lett. **29**(18), 2142–2144 (2004).
15. J. F. de Boer, B. Cense, B. H. Park, M. C. Pierce, G. J. Tearney, and B. E. Bouma, "Improved signal-to-noise ratio in spectral-domain compared with time-domain optical coherence tomography," Opt. Lett. **28**(21), 2067–2069 (2003).
16. R. Leitgeb, C. Hitzenberger, and A. Fercher, "Performance of fourier domain vs. time domain optical coherence tomography," Opt. Express **11**(8), 889–894 (2003).
17. B. R. Biedermann, W. Wieser, C. M. Eigenwillig, T. Klein, and R. Huber, "Dispersion, coherence and noise of Fourier domain mode locked lasers," Opt. Express **17**(12), 9947–9961 (2009).
18. B. R. Biedermann, W. Wieser, C. M. Eigenwillig, T. Klein, and R. Huber, "Direct measurement of the instantaneous linewidth of rapidly wavelength-swept lasers," Opt. Lett. **35**(22), 3733–3735 (2010).
19. R. Huber, M. Wojtkowski, K. Taira, J. Fujimoto, and K. Hsu, "Amplified, frequency swept lasers for frequency domain reflectometry and OCT imaging: design and scaling principles," Opt. Express **13**(9), 3513–3528 (2005).
20. D. C. Adler, W. Wieser, F. Trepanier, J. M. Schmitt, and R. A. Huber, "Extended coherence length Fourier domain mode locked lasers at 1310 nm," Opt. Express **19**(21), 20930–20939 (2011).
21. B. Potsaid, V. Jayaraman, J. G. Fujimoto, J. Jiang, P. J. S. Heim, and A. E. Cable, "MEMS tunable VCSEL light source for ultrahigh speed 60kHz - 1MHz axial scan rate and long range centimeter class OCT imaging," Proc. SPIE **8213**, 82130M, 82130M-8 (2012).
22. J. M. Schmitt, S. H. Xiang, and K. M. Yung, "Speckle in optical coherence tomography," J. Biomed. Opt. **4**(1), 95–105 (1999).
23. B. Považay, B. Hofer, C. Torti, B. Hermann, A. R. Tumlinson, M. Esmaeelpour, C. A. Egan, A. C. Bird, and W. Drexler, "Impact of enhanced resolution, speed and penetration on three-dimensional retinal optical coherence tomography," Opt. Express **17**(5), 4134–4150 (2009).
24. B. Potsaid, I. Gorczynska, V. J. Srinivasan, Y. L. Chen, J. Jiang, A. Cable, and J. G. Fujimoto, "Ultrahigh speed spectral / Fourier domain OCT ophthalmic imaging at 70,000 to 312,500 axial scans per second," Opt. Express **16**(19), 15149–15169 (2008).
25. L. An, P. Li, T. T. Shen, and R. Wang, "High speed spectral domain optical coherence tomography for retinal imaging at 500,000 A-lines per second," Biomed. Opt. Express **2**(10), 2770–2783 (2011).
26. R. Huber, M. Wojtkowski, K. Taira, J. G. Fujimoto, and K. Hsu, "Amplified, frequency swept lasers for frequency domain reflectometry and OCT imaging: design and scaling principles," Opt. Express **13**(9), 3513–3528 (2005).
27. W.-Y. Oh, B. J. Vakoc, M. Shishkov, G. J. Tearney, and B. E. Bouma, ">400 kHz repetition rate wavelength-swept laser and application to high-speed optical frequency domain imaging," Opt. Lett. **35**(17), 2919–2921 (2010).
28. B. Potsaid, B. Baumann, D. Huang, S. Barry, A. E. Cable, J. S. Schuman, J. S. Duker, and J. G. Fujimoto, "Ultrahigh speed 1050nm swept source/Fourier domain OCT retinal and anterior segment imaging at 100,000 to 400,000 axial scans per second," Opt. Express **18**(19), 20029–20048 (2010).
29. C. M. Eigenwillig, B. R. Biedermann, W. Wieser, and R. Huber, "Wavelength swept amplified spontaneous emission source," Opt. Express **17**(21), 18794–18807 (2009).
30. C. M. Eigenwillig, T. Klein, W. Wieser, B. R. Biedermann, and R. Huber, "Wavelength swept amplified spontaneous emission source for high speed retinal optical coherence tomography at 1060 nm," J. Biophotonics **4**(7-8), 552–558 (2011).
31. T. Klein, W. Wieser, C. M. Eigenwillig, B. R. Biedermann, and R. Huber, "Megahertz OCT for ultrawide-field retinal imaging with a 1050 nm Fourier domain mode-locked laser," Opt. Express **19**(4), 3044–3062 (2011).
32. V. J. Srinivasan, D. C. Adler, Y. L. Chen, I. Gorczynska, R. Huber, J. S. Duker, J. S. Schuman, and J. G. Fujimoto, "Ultrahigh-speed optical coherence tomography for three-dimensional and en face imaging of the retina and optic nerve head," Invest. Ophthalmol. Vis. Sci. **49**(11), 5103–5110 (2008).
33. W. Wieser, B. R. Biedermann, T. Klein, C. M. Eigenwillig, and R. Huber, "Multi-megahertz OCT: High quality 3D imaging at 20 million A-scans and 4.5 GVoxels per second," Opt. Express **18**(14), 14685–14704 (2010).
34. T. Klein, W. Wieser, R. Andre, T. Pfeiffer, C. M. Eigenwillig, and R. Huber, "Multi-MHz FDML OCT: snapshot retinal imaging at 6.7 million axial-scans per second," Proc. SPIE **8213**, 82131E, 82131E-6 (2012).
35. R. Huber, M. Wojtkowski, and J. G. Fujimoto, "Fourier Domain Mode Locking (FDML): A new laser operating regime and applications for optical coherence tomography," Opt. Express **14**(8), 3225–3237 (2006).
36. A. Oldenburg, F. Toublan, K. Suslick, A. Wei, and S. Boppart, "Magnetomotive contrast for in vivo optical coherence tomography," Opt. Express **13**(17), 6597–6614 (2005).
37. C. Blatter, T. Klein, B. Grajciar, T. Schmoll, W. Wieser, R. Andre, R. Huber, and R. A. Leitgeb, "Ultrahigh-speed non-invasive widefield angiography," J. Biomed. Opt. **17**(7), 070505 (2012).
38. E. Götzinger, M. Pircher, B. Baumann, T. Schmoll, H. Sattmann, R. A. Leitgeb, and C. K. Hitzenberger, "Speckle noise reduction in high speed polarization sensitive spectral domain optical coherence tomography," Opt. Express **19**(15), 14568–14585 (2011).
39. B. F. Kennedy, T. R. Hillman, A. Curatolo, and D. D. Sampson, "Speckle reduction in optical coherence tomography by strain compounding," Opt. Lett. **35**(14), 2445–2447 (2010).

40. F. Spöler, S. Kray, P. Grychtol, B. Hermes, J. Bornemann, M. Först, and H. Kurz, "Simultaneous dual-band ultra-high resolution optical coherence tomography," Opt. Express **15**(17), 10832–10841 (2007).
41. Y. Pan and D. L. Farkas, "Noninvasive imaging of living human skin with dual-wavelength optical coherence tomography in two and three dimensions," J. Biomed. Opt. **3**(4), 446–455 (1998).
42. M. Pircher, E. Gotzinger, R. Leitgeb, A. F. Fercher, and C. K. Hitzenberger, "Speckle reduction in optical coherence tomography by frequency compounding," J. Biomed. Opt. **8**(3), 565–569 (2003).
43. G. van Soest, M. Villiger, E. Regar, G. J. Tearney, B. E. Bouma, and A. F. van der Steen, "Frequency domain multiplexing for speckle reduction in optical coherence tomography," J. Biomed. Opt. **17**(7), 076018 (2012).
44. J. M. Schmitt, "Array detection for speckle reduction in optical coherence microscopy," Phys. Med. Biol. **42**(7), 1427–1439 (1997).
45. A. E. Desjardins, B. J. Vakoc, W. Y. Oh, S. M. Motaghiannezam, G. J. Tearney, and B. E. Bouma, "Angle-resolved optical coherence tomography with sequential angular selectivity for speckle reduction," Opt. Express **15**(10), 6200–6209 (2007).
46. M. Hughes, M. Spring, and A. Podoleanu, "Speckle noise reduction in optical coherence tomography of paint layers," Appl. Opt. **49**(1), 99–107 (2010).
47. A. E. Desjardins, B. J. Vakoc, G. J. Tearney, and B. E. Bouma, "Speckle Reduction in OCT using Massively-Parallel Detection and Frequency-Domain Ranging," Opt. Express **14**(11), 4736–4745 (2006).
48. Y. Watanabe, H. Hasegawa, and S. Maeno, "Angular high-speed massively parallel detection spectral-domain optical coherence tomography for speckle reduction," J. Biomed. Opt. **16**(6), 060504 (2011).
49. N. Iftimia, B. E. Bouma, and G. J. Tearney, "Speckle reduction in optical coherence tomography by 'path length encoded' angular compounding," J. Biomed. Opt. **8**(2), 260–263 (2003).
50. H. Wang and A. M. Rollins, "Speckle reduction in optical coherence tomography using angular compounding by B-scan Doppler-shift encoding," J. Biomed. Opt. **14**(3), 030512 (2009).
51. A. Wax, C. Yang, and J. A. Izatt, "Fourier-domain low-coherence interferometry for light-scattering spectroscopy," Opt. Lett. **28**(14), 1230–1232 (2003).
52. N. V. Iftimia, D. X. Hammer, R. D. Ferguson, M. Mujat, D. Vu, and A. A. Ferrante, "Dual-beam Fourier domain optical Doppler tomography of zebrafish," Opt. Express **16**(18), 13624–13636 (2008).
53. R. M. Werkmeister, N. Dragostinoff, M. Pircher, E. Götzinger, C. K. Hitzenberger, R. A. Leitgeb, and L. Schmetterer, "Bidirectional Doppler Fourier-domain optical coherence tomography for measurement of absolute flow velocities in human retinal vessels," Opt. Lett. **33**(24), 2967–2969 (2008).
54. Y.-C. Ahn, W. Jung, and Z. Chen, "Quantification of a three-dimensional velocity vector using spectral-domain Doppler optical coherence tomography," Opt. Lett. **32**(11), 1587–1589 (2007).
55. T. R. Hillman, A. Curatolo, B. F. Kennedy, and D. D. Sampson, "Detection of multiple scattering in optical coherence tomography by speckle correlation of angle-dependent B-scans," Opt. Lett. **35**(12), 1998–2000 (2010).
56. Y. Chen, D. L. Burnes, M. de Bruin, M. Mujat, and J. F. de Boer, "Three-dimensional pointwise comparison of human retinal optical property at 845 and 1060 nm using optical frequency domain imaging," J. Biomed. Opt. **14**(2), 024016 (2009).
57. R. Huber, D. C. Adler, V. J. Srinivasan, and J. G. Fujimoto, "Fourier domain mode locking at 1050 nm for ultra-high-speed optical coherence tomography of the human retina at 236,000 axial scans per second," Opt. Lett. **32**(14), 2049–2051 (2007).
58. M. Szkulmowski, I. Gorczynska, D. Szlag, M. Sylwestrzak, A. Kowalczyk, and M. Wojtkowski, "Efficient reduction of speckle noise in optical coherence tomography," Opt. Express **20**(2), 1337–1359 (2012).
59. B. J. Lujan, A. Roorda, R. W. Knighton, and J. Carroll, "Revealing Henle's fiber layer using spectral domain optical coherence tomography," Invest. Ophthalmol. Vis. Sci. **52**(3), 1486–1492 (2011).
60. W. Gao, B. Cense, Y. Zhang, R. S. Jonnal, and D. T. Miller, "Measuring retinal contributions to the optical Stiles-Crawford effect with optical coherence tomography," Opt. Express **16**(9), 6486–6501 (2008).

1. Introduction

Optical coherence tomography (OCT) is an interferometric imaging technique [1], which allows for cross-sectional imaging of a large variety of samples. OCT has applications, ranging from biomedical imaging to material studies, but today the most important application of OCT lies in ophthalmology. Since the first demonstration of its powerful diagnostic capabilities [2–4], OCT has rapidly become a standard ophthalmic imaging modality. Current research in retinal OCT technology focuses mainly on three aspects [5,6]: 1) Improved image quality, 2) high-speed imaging and 3) functional imaging. Progress has been made in each of the fields individually, but it should be noted that there is a close link between all of these aspects. In short, high-speed OCT enables novel approaches for image improvement and functional imaging. Unfortunately, too high speeds may in turn degrade image quality due to shorter exposure time. In the following, we will briefly discuss each of these three aspects in order to clarify their relevance and mutual dependence. Subsequently, we will present joint-aperture OCT (JA-OCT), a new approach which benefits all three aspects simultaneously.

Image quality is usually assessed by standard OCT system metrics, such as axial and transverse resolution, sensitivity and coherence decay, the latter of which is also known as sensitivity roll-off [7,8]. Each of these metrics can be optimized individually: Axial resolution on the order of a few microns has been achieved with ultra-high resolution OCT (UH-OCT) systems using broadband light sources [9,10]. Due to aberrations induced by the human eye, increased resolution in the transverse direction needs to rely on adaptive-optics OCT (AO-OCT) [11–14]. Another important metric is system sensitivity, which is defined as the minimum detectable fraction of back reflected light. There exists a fundamental physical limit to sensitivity, i.e. the shot noise limit, which can be reached in well designed OCT systems. Shot noise limited sensitivity increases linearly with power incident on the sample, and is inversely proportional to imaging speed. Thus, a 10x faster system will in general have a 10 dB lower sensitivity. However, it should also be pointed out that sensitivity is usually measured with the specular reflection from a mirror. Sensitivity values do therefore not reflect the collection efficiency of the back reflection from a sample, which in general is not a specular reflex, but rather has a wider angular distribution. We will show later how JA-OCT exploits this fact to increase collection efficiency at constant sensitivity. The introduction of Fourier domain OCT systems (FD-OCT) boosted sensitivity by several orders of magnitude compared to previous time-domain approaches [8,15,16]. FD-OCT can be further divided into spectrometer based OCT (SD-OCT) and swept-source OCT (SS-OCT). The main drawback of all FD-OCT techniques compared to TD-OCT is the limited imaging range, which is given by spectrometer resolution in SD-OCT and the instantaneous source linewidth or maximum electronic AD-conversion rate in SS-OCT [17–19]. It turned out that imaging range of SS-OCT can be far superior to SD-OCT, with the best available sources having imaging ranges of tens of millimeters [20,21]. In addition to those standard metrics, perceived image quality is strongly influenced by speckle noise. Speckle noise is inherent to all coherent imaging techniques, and results in a 100% noise-like modulation of the image [22]. One simple approach of speckle noise reduction exploits the speed of FD-OCT by averaging of multiple frames. Unfortunately, effective imaging speed is decreased drastically by frame averaging. For instance, consider a relatively fast FD-OCT system running at 100 kHz axial scan rate. Averaging of 20x frames reduces effective speed to 5 kHz, as slow as TD-OCT systems, which is not fast enough for the acquisition of larger 3D OCT data sets in-vivo. Finally, image quality may also be degraded by OCT signals from outside the sample, for instance by reflections from the sample arm imaging system. These parasitic signals may obscure the actual OCT signal from the sample, and cannot always be avoided in standard OCT systems.

Image quality and **speed** are closely interlinked by both sensitivity and averaging based speckle noise reduction, while resolution and roll-off are in principle speed-independent in FD-OCT. High speed is desirable for in-vivo imaging, since involuntary patient motion usually restricts image acquisition time to a few seconds [23]. Hence, faster systems can acquire much more data than slower systems in this restricted time. Historically, there were two large leaps towards higher speed OCT systems. First, SD-OCT pushed speed to several tens of kHz, which enabled high quality video-rate OCT [10]. Current commercial ophthalmic devices are based on SD technology and achieve axial scan rates of up to 50 kHz. The fastest experimental SD-OCT systems today are capable of imaging speeds of several hundreds of kHz [24,25]. The second leap towards higher speed occurred with the introduction of fast SS-OCT systems. In SS-OCT, axial scan rates are given by the repetition rate of the wavelength swept laser. With standard short cavity lasers, speed is limited by the buildup time for lasing at each wavelength [26], and the highest achievable speeds are a few hundred kHz [27,28]. One solution for increased speed are filtered amplified spontaneous emission (ASE) sources [29], which have also been used for retinal imaging at up to 340 kHz axial scan rate [30]. The introduction of even higher speeds is highly desirable for a variety of reasons, including densely sampled imaging of the retina over very large fields of view [31,32]. Axial scan rates in the multi-MHz range have been demonstrated with Fourier domain mode-locked (FDML)

lasers [31,33,34]. FDML overcomes the speed limit of conventional tunable lasers by synchronization of cavity round trip time and wavelength filter tuning rate [35], which is strongly dependent on cavity dispersion [17,20].

Functional imaging increases the diagnostic capabilities of OCT by providing complimentary contrast. The various functional OCT approaches can be classified according to the specific contrast mechanism that is used. Interestingly, in many functional techniques contrast is formed by analysis of the speckle pattern or phase of the OCT signal, both of which are involuntarily altered by sample or system movement. Therefore, many functional OCT techniques profit from very high imaging speeds, since the resulting short acquisition times "freeze" the contrast-degrading motion of the sample. Examples for speckle-sensitive techniques are magnetomotive OCT for molecular contrast [36], and speckle variance OCT for blood flow visualization [37]. Moreover, functional imaging techniques do usually slow down the acquisition process, since many times multiple scans have to be acquired at the same position to evaluate the changing speckle or phase pattern. In order to cover the same sample areas as standard systems, much higher speeds are therefore necessary [37]. Additionally, averaging of multiple scans can improve image quality considerably, for example in polarization sensitive OCT [38]. This is equivalent to standard OCT frame averaging, and again, high speed systems facilitate averaging but do decrease sensitivity due to their smaller exposure time per axial scan.

In summary, image quality, speed and functional imaging are intrinsically connected. Specifically, high speed is crucial for phase sensitive and speckle variance techniques. Despite its usefulness for functional imaging, the speckle pattern itself is usually perceived as detrimental to image quality. Hence frame averaging is commonly used in commercial OCT systems to reduce speckle noise, but this method reduces effective imaging speed drastically, compromising the ability to acquire data sets over larger volumes. However, highest speeds on the order of MHz may seem too fast for practical application, considering that obtainable sensitivity is limited by maximum permissible exposure. Additionally, usual hardware-based speckle reduction techniques are not compatible with high-speed and/or in-vivo imaging, as we will discuss in the next section.

Thus, the challenge is to construct an OCT system that does not compromise speed for speckle reduction and intrinsic functional OCT capabilities. Here we present joint-aperture OCT (JA-OCT), an angle-resolved OCT technique operating at 1.68 MHz axial scan rate. Contrary to other angle-resolved OCT techniques, JA-OCT is compatible with high-speed in-vivo retinal OCT and increases, at the same time, the collection efficiency of the system. In addition to higher collection efficiency, JA-OCT further improves image quality by parasitic signal suppression and speckle reduction through parallel angular compounding. JA-OCT also offers new possibilities for functional imaging such as angle-resolved Doppler OCT.

2. Theory: Hardware speckle reduction, collection efficiency and JA-OCT

In this section, we describe JA-OCT and discuss how it relates to other speckle reduction techniques as well as to OCT systems with large numerical aperture (NA), e.g. adaptive optics OCT (AO-OCT). For this purpose, we will briefly discuss speckle formation and hardware based speckle reduction techniques. Subsequently, the concept of JA-OCT will be presented. Finally, the increased collection efficiency and parasitic signal suppression of JA-OCT will be discussed.

2.1. Hardware based speckle reduction techniques and JA-OCT

One advantage of JA-OCT is the ability of speckle reduction at the system's full speed. Speckle may impede the correct interpretation of structural features in OCT. There are two different strategies to reduce speckle noise: software and hardware based techniques [22]. Software based techniques take the speckled OCT image as input, and process the image in a way that gives it a smoother appearance. The prototype software speckle reduction technique

is downsampling, i.e. local averaging of adjacent pixels. This already illustrates the main issue software based techniques: Since no additional information about the sample can be obtained after image acquisition, the resolution of the resulting despeckled image is usually degraded and the image appears less crisp.
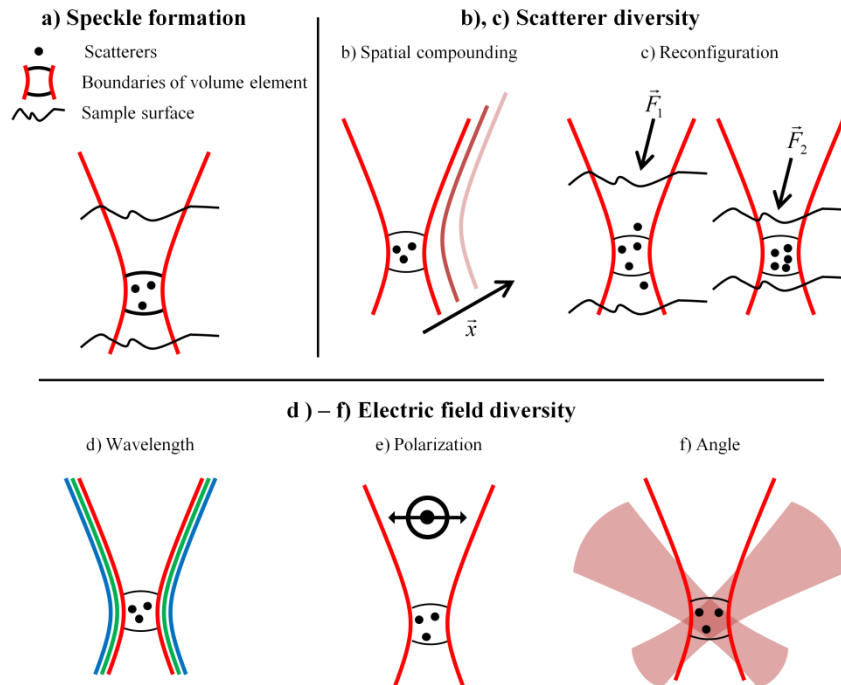

Fig. 1. a) Speckle is formed by superposition of the electric fields from scatterers in each resolvable volume element. b)-f) Speckle reduction: b) In spatial techniques, speckle patterns from different locations are compounded, yielding speckle reduction at the cost of reduced (transverse) resolution. c) Scatterer diversity may also be achieved by induced motion of the scatterers. d) Wavelength diversity employs incoherent compounding of the speckle pattern formed at different wavelengths. e) Polarization diversity can also achieve speckle reduction. f) Since the speckle pattern looks different from every angle, speckle can be reduced by angular compounding. JA-OCT uses this angle-anisotropy to combine active illumination with passive probe channels.

Hardware based techniques, on the other hand, do obtain additional information about the sample in order to reduce speckle noise. The key to hardware based techniques is speckle pattern diversity, i.e. the combination of images showing different speckle patterns. Note that speckle reduction is an incoherent process, in which only the intensity of the OCT image is used. Figure 1a illustrates the speckle formation process. In OCT, a resolvable volume element is limited by the transverse beam width and the axial resolution. While the axial resolution remains constant, the beam width and thus the size of the volume element varies with sample position. Speckle is formed because OCT cannot resolve scattering sub-structures ("scatterers") within each resolvable volume element. In a simplified model, consider M scatterers in a volume element. The total reflected field E_{out} is the coherent superposition of the individual scattered fields from each of these M scatterers. Thus the amplitude of E_{out} varies between 0 and a maximum value depending on the relative phase of each of the scattered fields. The key to hardware based speckle reduction is the variation of the relative phases of the scattered fields, since different phases will result in different speckle patterns.

In general, the phase of the scattered field depends on both the microscopic configuration of the scatterers, the incoming electric field and the direction of the outgoing field. Speckle

pattern diversity can thus be obtained by diversity in scatterer configuration as well as by diversity in electric field. There are five main speckle reduction techniques (Figs. 1b-1f):

a) *Spatial compounding*: Voxels from different locations in the sample are averaged to reduce speckle noise at the cost of resolution. Examples include B-frame averaging and isotropic averaging [31].

b) *Scatterer reconfiguration*: Instead of changing the scan location, the phase from each scatterer in the resolvable volume can also be varied by reconfiguration of the scatters, for instance by translation, rotation or chemically induced changes. Examples of scatterer reconfiguration include magnetomotive OCT [36] and strain compounding [39]. Like spatial compounding, scatterer reconfiguration methods always need at least two successive scans at the same location, i.e. at least one scan for each scatterer configuration.

c) *Wavelength diversity*, usually called frequency compounding. Speckle reduction is achieved by averaging of images obtained with different wavebands. Separation into different wavebands is either performed in hardware with separate detection channels [40–42], or in software by numerical separation [43]. Both methods have the drawback of limited number of uncorrelated speckle patterns: With parallel detection, the number of wavebands is usually limited to two, since complexity in optical design, detection and source(s) increases rapidly [42]. Moreover, usually only a few distinct wavebands offer a good balance of scattering and absorption, such as the 850nm and 1060nm wavebands used for retinal imaging. Additional wavebands in regions of low penetration or signal would only offer minor improvement. In numerical separation methods, axial resolution decreases rapidly with number of wavelength sub-bands, such that these methods are sometimes only applied to aid segmentation, and not for general image display [43].

d) *Polarization diversity*: Using polarization-resolved methods speckle reduction is achieved by compounding signals from different polarization channels. This technique is not commonly used as the amount of speckle reduction is limited.

e) *Angle diversity*: Angle diversity relies on both the angular dependence of the scattering amplitude and phase, and the angular variation of the optical path lengths from the different scatterers at the point of interference. Using angular compounding, high-quality speckle reduction has been demonstrated, starting with the work of J. Schmitt [22,44]. Angle resolved methods can be divided into sequential and parallel approaches. In sequential approaches, the incident angle is varied step by step [45,46], which makes these approaches unsuitable for in-vivo imaging of unsteady samples, for instance the human eye. In parallel approaches, the sample is usually illuminated with a single high NA beam, and angle is encoded in a specific domain. Examples include spatial encoding and array detection [44,47,48], path-length encoding [49] and Doppler frequency shift encoding [50]. Most encoding domains degrade the OCT signal: Array approaches are prone to poor sensitivity due to detector noise, cross-talk and/or lower spectral resolution, whereas path length encoding suffers from sensitivity roll-off and decreased imaging range.

Note that all scatterer diversity techniques are prone to degradation of structural information: In spatial diversity, resolution is degraded, whereas scatterer reconfiguration directly changes the structure of the sample. Regarding the electric field diversity techniques, wavelength and polarization diversity techniques usually suffer from the small achievable number of different speckle patterns, which is limited by practical reasons. So, angular diversity seems to be the only hardware based technique which does not degrade structural information, and provides a possibly very large number of uncorrelated speckle patterns.

2.2. Implementation of angle-resolved detection by joint aperture OCT

JA-OCT is a parallel angle-resolved technique, which is specifically tailored to ultrahigh-speed OCT systems. JA-OCT combines illumination from a standard active OCT channel with passive detection on a multitude of additional passive channels (Fig. 2). The active channel is equivalent to the single channel in a standard OCT system. In contrast, no light is incident on the sample from the passive channels, which only collect light that is backscattered under an angle with respect to the beam from the active channel. This multiplexed approach combines the advantages of angle-resolved detection without sacrificing imaging speed. Moreover, the collection efficiency and thus the effective sensitivity of the OCT system are increased, and the quality of the OCT signal from the active beam is not compromised. Both aspects are very important for ultrahigh-speed OCT systems, which already suffer from relatively low signal levels due to lower exposure time.

JA-OCT has advantages over other angle-resolved methods. In setups using multiple active beams, which are incident on the same sample position under different angles it is difficult to assess exact beam alignment: Due to active illumination for every channel, an OCT signal is detected for all channels even with bad alignment. In contrast, in JA-OCT an OCT signal can only be detected if the passive channels are perfectly aligned. In other parallel approaches, the numerical aperture (NA) is the same for illumination and detection, which is often a direct consequence of the underlying free-space interferometer layout [44,47,48]. Thus, the confocal gate is either not present at all [44,47,48], which leads to signal-degrading cross-talk, or the confocal gate is the same for all angles [49,50], such that the scattering direction is not unambiguously defined. Moreover, a multitude of additional information is available with JA-OCT:

- Measurement of the angular dependence of scattering, which may be useful for automatic tissue identification [51]. Note that this information is different to information from previously presented angle-resolved techniques, in which only light backscattered within the NA of the incoming beam(s) can be detected.

- Suppression of the specular reflex and of parasitic reflections from sample arm optics. By definition, the specular reflex can only be present in one of the multiple channels in JA-OCT. Therefore, parasitic reflections from the sample arm optics only affect one channel, which is usually the active channel.

Finally, JA-OCT shares, in principle, all the benefits of other angle-resolved techniques:

- Estimation of the true three-dimensional velocity vector in Doppler OCT [52–54].

- Detection of multiple-scattering by speckle correlation of scans acquired from multiple angles [55].
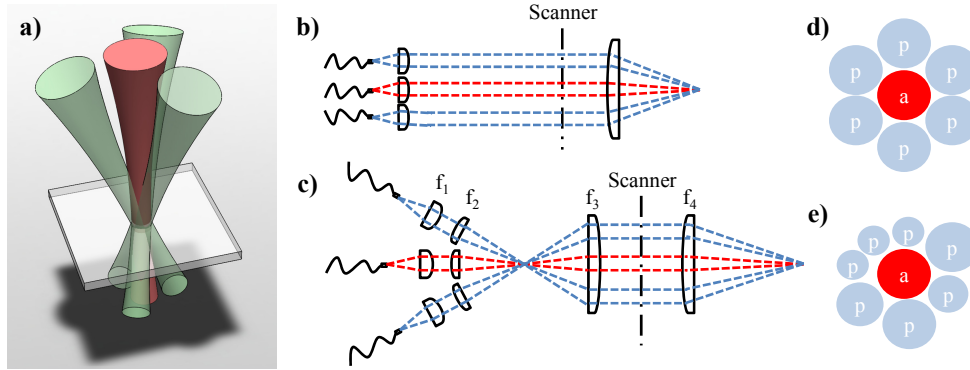
Fig. 2. In joint aperture OCT (JA-OCT), the sample is illuminated by one active beam and additionally probed by passive beams. a) Rendering of a symmetric JA-OCT geometry with active center beam and three probe beams. b,c) Schematic sample arm configurations for JA-OCT. An intermediate focus may allow for more flexible beam alignment, since the lenses may have a larger distance between each other. d) If all beams have the same size, dense packing allows for a maximum of 6 probe beams surrounding the active beam. e) However, JA-OCT is neither restricted to a symmetric configuration nor to beams of the same size. a: active (illuminating) beam; p: passive (probe-only) beam.

2.3. Increased collection efficiency and sensitivity of JA-OCT

In this section, we discuss the increased collection efficiency of JA-OCT, and present an intensity threshold for increased sensitivity with the additional passive channels. In addition to the information gained from multi-angle detection, JA-OCT increases the collection efficiency of the detection system due to the collection of additional photons by the passive channels. In contrast, approaches with multiple active beams incident on the same sample location do not increase collection efficiency [52–54]. This is a main drawback in connection with high speed OCT, since maximum permissible exposure needs to be divided between all active channels, which may lead to lower than acceptable sensitivities on each of these channels. For instance, in retinal imaging sensitivity should not be much below 90 dB, given a total retinal reflectivity of ~-60 dB and typical dynamic range of ~25 dB [56]. In retinal imaging, this limit is reached at speeds of more than 1 MHz, as used in our system.

It may be argued that collection efficiency of JA-OCT cannot be higher than the one of a system with equivalent NA. However, one needs to take into account that aberrations of the imaging system affect each of the channels separately, and that the single channels have a relatively low NA. This means that the beams of each channel pass only a small fraction of the total aperture of the optical system. Hence, the effect of aberration can be reduced by adjusting the relative orientation of each passive beam individually (Fig. 3). JA-OCT thus gives control over the compound return in a manner similar to AO-OCT, where the wavefront is also adjusted locally in order to correct for aberrations, increasing collection efficiency. However, JA-OCT is easier to implement, since only the active beam illuminates the sample. Thus, constructive interference of the incoming wavefront as in AO-OCT is not necessary. Hence only the relative orientation of the wavefronts and not their relative phases need to be corrected in JA-OCT. The absence of the constructive interference condition is closely related to the connection between incoherent and coherent angle compounding in AO-OCT and JA-OCT.

Compared to smaller apertures, transverse resolution is higher in systems with large NA / AO-OCT, corresponding to a smaller speckle size. The reduced speckle size is due to the *coherent* interference of a large number of angular components of the incoming wavefront. Albeit speckle size is smaller, modulation depth of the speckle pattern is not changed. In JA-OCT, the angular components are detected separately and added *incoherently*, leading to a reduction of speckle noise.

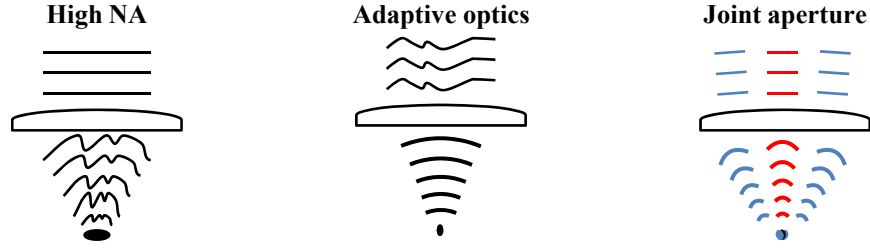| High NA	Adaptive optics	Joint aperture

Fig. 3. Comparison of standard high numerical aperture (NA), adaptive optics (AO) and joint aperture (JA) confocal imaging. In each case, the figure shows the incoming wavefront, a focusing lens, and the converging wavefront to one sample location. In high NA imaging, lens aberrations induce more and more wavefront distortion as NA is increased. Thus, the imaging system reaches maximum collection efficiency at an NA value that is given by the specific imaging system. With adaptive optics, the incoming wavefront is predistorted in order to compensate for aberrations, enabling the use of very large NAs. JA imaging is conceptually similar to AO imaging, since each beam can easily be tilted individually in order to correct for aberrations. Note that, contrary to high-NA and AO methods, the relative phase across the NA does not need to be actively controlled, since it is already set by the active (illuminating) beam.

Note that resolution can be sacrificed for reduced speckle-noise in AO-OCT images, for instance by transverse downsampling. However, this downsampling step reduces effective imaging speed by the chosen downsampling factor, whereas the full imaging speed is always maintained in JA-OCT.

2.4. Signal increase by n-channel passive JA-detection

JA-OCT relies on the fact that reflection is in general diffuse, and not only specular. The exact angular characteristics of back reflection depend on the sample type. For JA-OCT, it is important that sufficient power is collected by the passive channels such that speckle reduction is effective and sensitivity is increased. This imposes a threshold on the relative fraction α of power collected by the passive channels. By adding the signal of N channels, the amplitudes add up linearly, whereas the standard deviation of noise increases with the square root of N. Hence, signal-to-noise ratio SNR_N (peak to standard deviation) of the averaged signal increases compared to single channel SNR if

$$\frac{SNR_N}{SNR} = \frac{\sum_{i=1}^{N} \alpha_i}{\sqrt{N}} \stackrel{\alpha_i = const.}{=} \frac{1 + \alpha(N-1)}{\sqrt{N}} > 1, \qquad (1)$$

where N is the total number of channels including one active channel, and α_i is the ratio of power in passive channel with index i to the power in the active channel with index 1 (i.e. $\alpha_1 = 1$ by definition). Assuming for simplicity that α is equal for all passive channels, we get

$$\alpha > \frac{\sqrt{N}-1}{N-1} \xrightarrow{N \to \infty} \frac{1}{\sqrt{N}}. \qquad (2)$$

As expected, the necessary relative power collected by the passive channels decreases with the square root of the number of channels for large N. For small N, the threshold α is slightly larger. For instance, $N = 4$, as in our case, implies $\alpha > 0.58$, i.e. the signal of the passive channels should not be weaker than -2.4 dB of the active channel signal. Note that this discussion is valid not only for JA-OCT, but for all OCT modalities in which incoherent (image magnitude) averaging of frames with unequal signal strength is performed.

3. Methods

3.1. Experimental setup

Figure 4 shows the interferometer layout of the four channel JA-OCT system. We used a 1050nm FDML laser [31,57], running at a fundamental frequency of 419 kHz, which was increased to 1.68 MHz in an external 4x buffering stage. After the buffer stage, a booster amplifier cleaned up the polarization state and passively shaped the buffered sweeps to a roughly Gauss-like shape. With a total sweeping range of ~70nm, we measured an axial resolution of ~14 μm in air. We chose a Michelson interferometer layout for the active channel, and a Mach-Zehnder configuration for the passive channels, such that reference arm power is provided to the passive channels, while only the active channel illuminates the sample. The main building block for all channels is a symmetric combination of standard fiber couplers (AC-Photonics) for spectrally flat response [31]. Note that the use of special and ~10x more expensive spectrally flat couplers may render the insertion of the additional couplers obsolete for the passive channels, increasing sensitivity by another ~3 dB. For the passive arms, N-BK7 right angle prisms were used as retroreflectors, tilted by a few degrees in order to suppress fiber-coupling of residual reflections. An equal amount of glass was inserted into the reference arm of the active channel, compensating sample-arm dispersion. For each channel, we used an AC-coupled, differential photoreceiver with 1 GHz analog bandwidth (Wieserlabs WL-BPD1GA) in combination with a low-pass filter (Mini-Circuits BLP-450 +). 150 μW to 200 μW optical power from the reference arm was incident on each of the two photoreceiver inputs, and 1.7 mW was incident on the sample. For the active channel, we measured a sensitivity of 90 dB, which is only 0.5 dB below the shot noise limit, considering 50% measured backcoupling efficiency and 3 dB additional interferometer loss. The relatively low backcoupling efficiency is partly due to losses in the multi-channel sample arm, as will be discussed later.
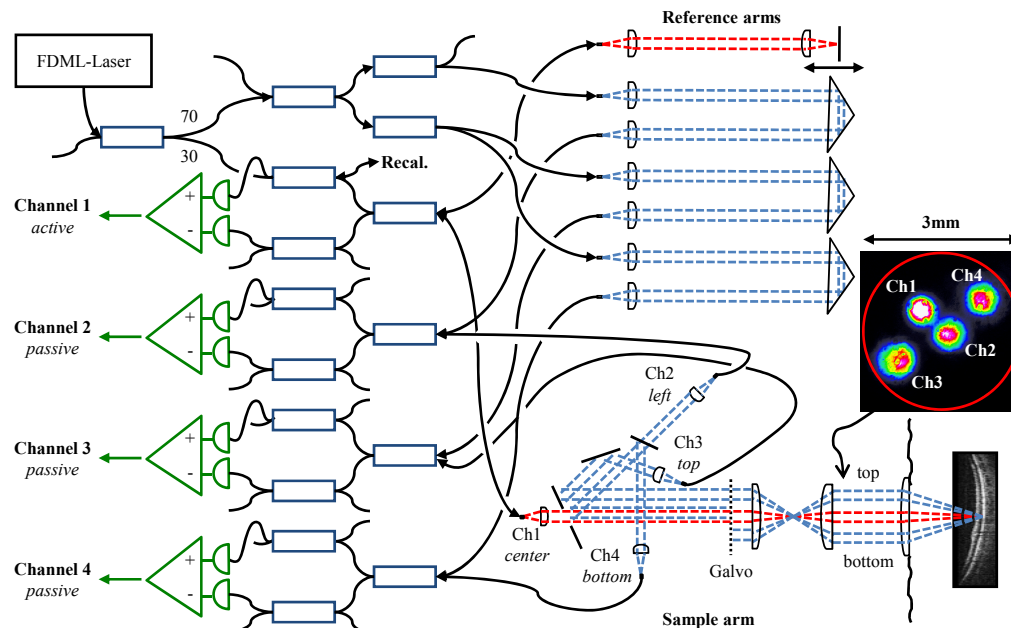

Fig. 4. JA-OCT interferometer layout. Square boxes represent 3dB fiber couplers, unless the coupling ratio is indicated individually. Fiber based polarization controllers are present in each sample and reference arm (not shown). Note that the direction of view in the sample arm is switched from top view to side view at the galvanometer mirrors in order to better visualize the beam geometry. Inset: Beam profile in front of the eye, with light coupled to all channels. All beams are located in a circular aperture (red) of 3mm diameter.

Analog-to-digital conversion of all channels was performed with a single 8bit, 4 channel PCIe digitizer card at 4 x 1.5GS/s (Signatec PX1500-4). The digitized data was stored on the digitizer card memory (2 GB size), and transferred to the host PC memory after data acquisition. In principle, the free-space sample arm configuration corresponds to the one shown in Fig. 2b). All beams are collimated with aspheric lenses of 7.5 mm focal length (Thorlabs A375-C). Measured beam diameters are 1.3 mm (86.5% power). The passive beams are located on top, side and bottom of the active beam for beams 2-4, respectively. The active and passive beams are combined on a custom mirror with a central, circular aperture of 1.9 mm diameter. The beam from channel 1 is slightly focused through this aperture, losing 5% power. For alignment, light was coupled into the passive channels, and channels 3 and 4 are inserted next to the channel 2 beam with the help of D-shaped mirrors (Thorlabs PFD10-03-P01), losing ~10% power. After passing the mirror edges, slight diffraction patterns can be observed on all beam profiles (Fig. 4 inset). Back-coupling efficiency is not strongly affected by diffraction, as measured for channel 1. In addition to the 5% loss at the circular aperture, ~15% power are lost at the galvanometer mirrors, the lenses and the folding mirror, leading to a free-space to fiber coupling efficiency of ~62%.

After the circular mirror, the distance from the center of channel 3 to the center of channel 4 is ~3.8 mm, and all beams pass the galvanometer scanner aperture of ~6 mm. The relay telescope further decreases this distance by about a factor of two, such that all beams are located inside a circular aperture of less than about 3 mm diameter, suitable for imaging of the non-mydriatic human eye (see Fig. 4 inset). The diameter of the illuminating beam is about 0.6 mm directly in front of the eye. For transverse beam scanning, standard galvanometer scanners (Cambridge Technologies 6215H) were used. On the fast axis, the scanners followed a linear ramp with a duty cycle of 70%, in order to provide sufficient fly-back time, during which no data was recorded.

3.2. Data processing

Standard OCT data processing was applied to each channel separately. First, a fringe trace is recorded for the active channel only with the help of an additional recalibration arm, and the time to wavenumber (k-space) mapping for each buffered sweep of the FDML laser is calculated. Second, data is sinc-interpolated by zero padding using Fourier transforms. Then, time to k-space resampling is applied to every channel with the time to k-space mappings from the active channel. Finally, numerical dispersion compensation is applied to each channel individually [58], and the fringe signals are Fourier transformed. For image display, 20*log of the magnitude of the Fourier transform is taken. Values below a low cut level are set to black, and values higher than the high cut level are displayed as white, with grey values corresponding to intermediate values. The cut levels were set automatically: The low cut level was set to the mean of the noise floor, and the high cut level was 25 dB larger than the low cut level. The automatic cut-level determination facilitates inter-channel comparability despite slightly varying reference arm powers. Finally, images were gamma-adjusted for better screen-visualization. Averaging and compounding were performed after logarithmization.

4. In-vivo retinal imaging

4.1. Imaging results and averaging

Figure 5 and Fig. 6 show in vivo imaging examples of the human retina with the JA-OCT setup. For all OCT measurements, we acquired 2112x258 axial scans for each channel in a total time of 0.46 s, including galvanometer scanner dead time. Before data acquisition, the directions of all passive beams where adjusted online for maximum signal. Movement of the sample necessitates re-adjustment of all channels.
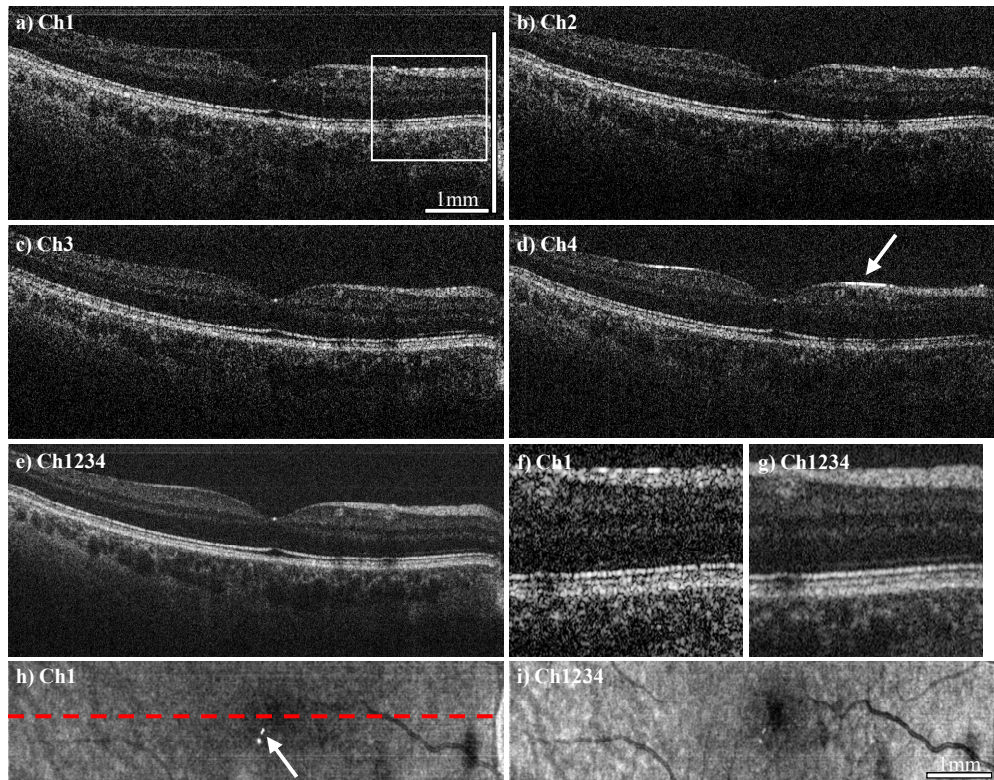
Fig. 5. a-d) OCT B-frame tomograms from channel 1 to 4, consisting of 2112 axial scans, acquired at 1.68 MHz axial scan rate. e) Compounded tomogram (average of all channels), exhibiting improved image quality. f,g) Zoomed region of interest (ROI) of channel 1 and the compound tomogram, at the position indicated by the white box in a). Speckle reduction in the compounded image is clearly visible. Also note the increased visibility of the retinal layers, for instance of the external limiting membrane (ELM). Reflection from the ELM seems to be angle-dependent, with most of the signal in this region stemming from channel 3. h,i) En-face views of the complete data set (256 frames), indicating the position of the B-frames with the dashed red line. JA-OCT clearly reduces the impact of both specular reflections from the sample (see arrow in Ch4) and of parasitic reflections, which originate from the sample arm lenses (see arrow in the en-face view of Ch1). Scale bar length is 1mm in tissue (assuming n = 1.33, 0.288 mm/degree scan angle).

The acquired data set shows all benefits of JA-OCT: 1) Speckle reduction, 2) increased collection efficiency, 3) reduction of specular and parasitic reflections. Figures 5a-5d show B-frames from all channels. Variation between the individual speckle patterns is clearly visible. Hence, the compound image (Fig. 5e) has a much smoother appearance. Better visualization of retinal layers (Figs. 5f, 5g) is not only due to speckle reduction, but also due to higher signal-to-noise ratio (SNR) of the compound image compared to the single images. The increased SNR is due to increased collection efficiency of JA-OCT. We assessed the increased collection efficiency by analyzing the energy content of the images from each frame. For this purpose, we computed the average intensity of all pixels in the logarithmic intensity images that were at least 8dB above the mean noise value. For channels two, three and four, the average intensity was 1.4 dB, 1.3 dB and 2.1 dB below the average intensity of channel 1, respectively. See section 4.2. for further discussion on SNR increase. Visualization of retinal structure also benefits from angular compounding, because some layers show angular dependence of scattering. For instance, the strongest signal from the external limiting membrane in the zoomed region of interest (ROI) is found in channel 3. Since specular reflection is by definition strongly angle dependent, a specular reflex will in general only be

visible in one channel, as can be seen in Fig. 5d. Hence, specular reflections are not visible in the compounded tomogram, except for the central fovea. At this location, all channels show a specular reflex due to the strongly varying curvature of the retina. A closer inspection shows that these specular reflections are not exactly at the same position, but slightly offset from each other. The en-face visualization of the entire data set reveals the reduction of parasitic reflections in the compound image. Moreover, the increased SNR leads to far better visibility of the retinal structure. For further speckle reduction, JA-OCT can be readily combined with standard frame averaging. Here, we averaged adjacent frames from the 3D data set three to 24 times. As can be seen in Fig. 6, the compound images always show much less speckle noise than the averaged frames from a single channel. Due to the very high speed of our MHz-OCT system, no alignment of the adjacent frames was necessary.
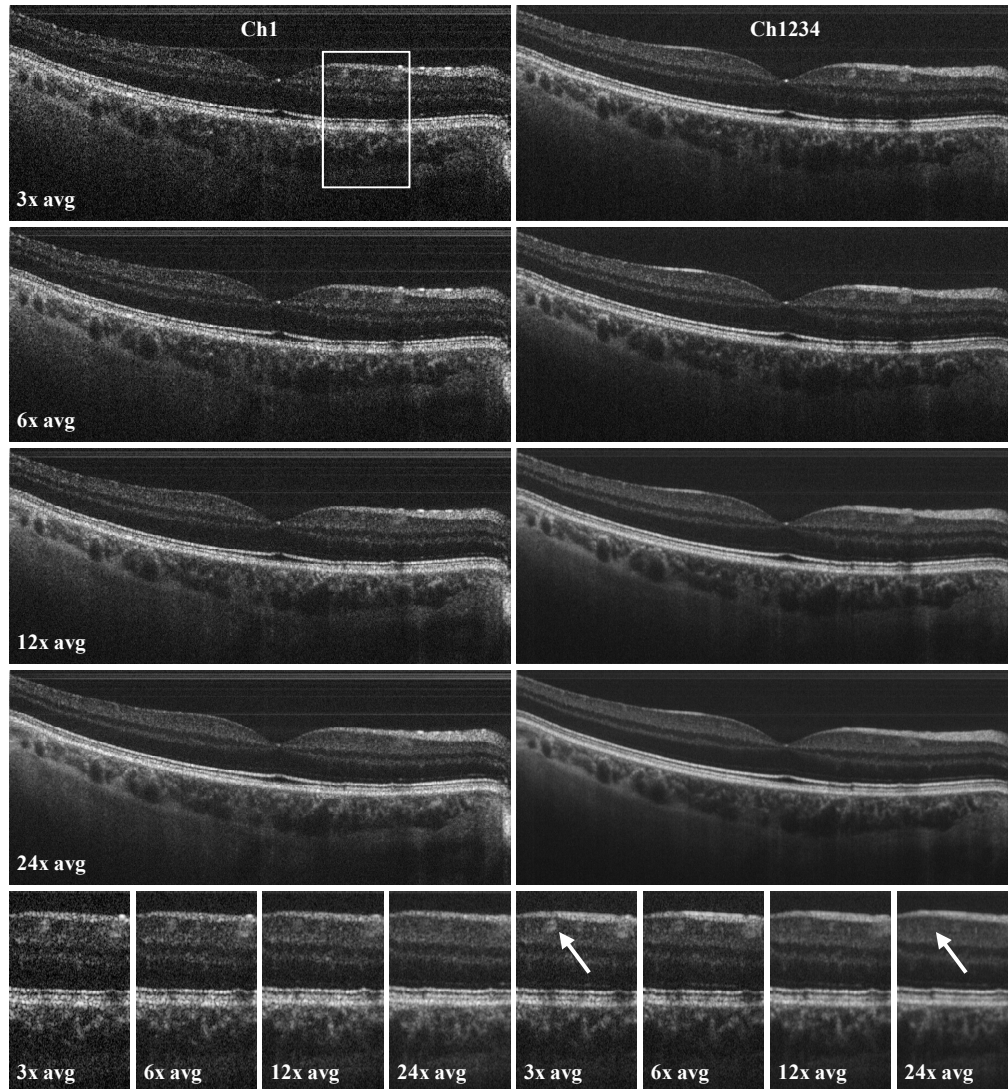

Fig. 6. Averaging of adjacent frames in standard single-channel OCT (left) and JA-OCT (right), at the same location as in Fig. 5. Image quality of the compounded JA-OCT images is always superior to single-channel imaging. Bottom: In the enlarged image sections, it can be clearly seen that averaging of frames spanning less than 100 μm distance already blurs out important image detail, such as the blood vessel indicated by the arrow.

Moreover, it can be seen that the original speckle pattern remains fairly stable even for large number of averaged frames. In fact, image blur due to transverse structural decorrelation may occur in some regions of the OCT scan before the speckle pattern becomes completely decorrelated in other parts of the OCT scan. For instance, a blood vessel to the right to the fovea is clearly visible in the 3x – 6x averaged frames, but barely visible in the 24x averaged frame. This is due to the fact that the orientation of this blood vessel is almost perpendicular to the orientation of the averaging direction, as can be seen in the en-face view in Fig. 5i. In contrast, other regions in the image are still affected by speckle noise, and angle-compounding still produces a smoother appearance even for high number of averaged frames. Note that spacing between two B-frames in only about 4.3 μm, such that total distance between frames is less than 100 μm even for 24x averaging, which is less than an optimum distance of 110 μm as reported by Szkulmowski et. al. [58]. Hence information about structures orientated perpendicularly to the scan direction is already lost before optimum frame separation for speckle contrast is reached. In contrast, JA-OCT already produces high quality, speckle reduced images with only moderate averaging at 1.68 MHz axial scan rate, leading to very high effective imaging speeds of hundreds of kHz for high quality, speckle-reduced images.

4.2. Signal to noise ratio

Speckle noise reduction can be quantified by the signal-to-noise ratio (SNR) of the image, which is defined as $SNR = \langle I \rangle / \sigma$, where $\langle I \rangle$ and σ are the mean and standard deviation of the power level [22]. For SNR analysis, we first computed the square of the linear FFT magnitude. Second, the noise level was normalized for all channels to account for varying reference arm power and detector responsivity. We assessed relative power in the passive channels in a region of interest (ROI) around the RPE (Fig. 7a). The relative power in the ROI was 0.82, 0.73 and 0.55 for channels 2, 3 and 4, respectively (Fig. 7b). For equal powers and completely uncorrelated speckle patterns, the SNR should increase with the square root of the number of averages. In our case, the increase in SNR is lower, since the power level in the passive channels is lower than in the active channel (Fig. 7c). Compared to the single active channel, the measured SNR for the average of all channels increases by a factor of 1.4, from 0.30 to 0.42. Using the relative power levels, Eq. (1) predicts an increase by a factor of 1.56. The difference to the measured value can be attributed to partial correlation between the speckle patterns.
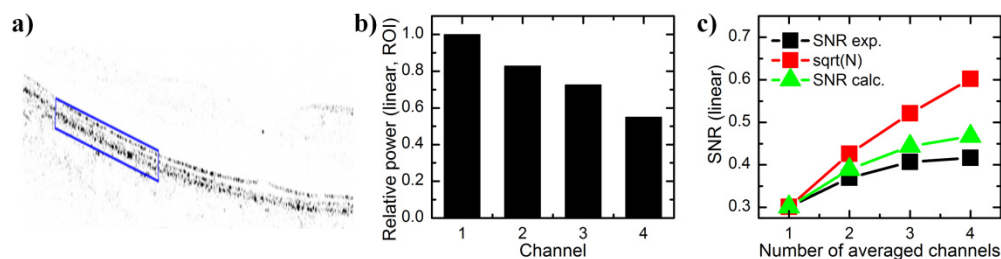

Fig. 7. a) Retinal image with inverse contrast and in linear power scale (FFT signal squared). Blue box indicated region of interest (ROI) around the RPE layer. b) Mean signal power in the ROI with respect to the power in the active channel 1. c) Signal-to-noise ratio (SNR) calculated as power mean to power standard deviation over the entire image (black squares). Since the signal is weaker in the passive channels, the SNR increase is lower than with the square root of channel number (black squares). The experimental SNR increase is close to the calculated value (green triangles), which takes into account the varying power levels, assuming completely uncorrelated speckle patterns (Eq. (1)).

5. Conclusion and outlook

In this work we have demonstrated angle-resolved in-vivo imaging of the human retina with more than two channels, introducing joint-aperture detection. JA-OCT offers numerous benefits, which are especially relevant for ultrahigh-speed systems: The increased collection efficiency of JA-OCT can partially compensate for lower exposure time per line. Additionally, maximum permissible exposure is not divided between multiple active channels, but concentrated on the single active illumination channel. A division of incident power between multiple active channels would lead to unacceptably low sensitivity values at ultrahigh speeds as presented in this paper. Moreover, image quality in JA-OCT is further improved by channel compounding for speckle reduction. Speckle reduction can be further increased by standard frame compounding. Since the speckle noise is already reduced by angle compounding, a relatively small number of ~10 frames are sufficient to generate very smoothly appearing images. Hence, effective imaging speed *with 10x frame averaging* is still 168 kHz, even faster than the raw frame rate of all commercial and most research OCT systems.

Further studies using JA-OCT may investigate visibility of directionally reflecting layers such as Henle's fiber layer [59]. Directional reflectivity in other retinal layers, known as optical Stiles-Crawford effect and caused by the waveguiding property of the photoreceptors, can also be observed with angle-resolved OCT [60]. For retinal imaging, the passive beams need to be realigned actively in order to compensate for aberrations that vary with eye position, in analogy to the constant readjustment of the deformable mirror in AO-OCT. This constant readjustment complicates in-vivo retinal imaging. In future, the alignment process may be automated, using motorized mirror mounts and optimizing for signal intensity of each channel separately. JA-OCT also offers new perspectives for functional imaging: Increased information may be used for speckle-variance based angiography, and phase analysis of all channels may allow for reconstruction of the true Doppler vector. Finally, tissue identification using the angular scattering characteristics may be feasible, especially with larger number of detection channels.